

Article

Investigation of the Interface between Laser-Melted CoCr and a Stainless Steel Substrate

Cosmin Cosma¹ , Christina Teusan², Peter Gogola³ , Mihaela Simion⁴, Zuzana Gabalcova³ , Adrian Trif¹, Petru Berce¹  and Nicolae Balc^{1,*}

¹ Department of Manufacturing Engineering, Technical University of Cluj-Napoca, 400641 Cluj-Napoca, Romania; cosmin.cosma@tcm.utcluj.ro (C.C.); adrian.trif@tcm.utcluj.ro (A.T.); petru.berce@tcm.utcluj.ro (P.B.)

² MAN Truck & Bus SE, 80995 Munich, Germany; christina-valentina.teusan@man.eu

³ Faculty of Materials Science and Technology in Trnava, Materials Science, Slovak University of Technology in Bratislava, 91724 Trnava, Slovakia; peter.gogola@stuba.sk (P.G.); zuzana.gabalcova@stuba.sk (Z.G.)

⁴ Department of Strength of Materials, Technical University of Cluj-Napoca, 400641 Cluj-Napoca, Romania; mihaela.simion@rezi.utcluj.ro

* Correspondence: nicolae.balc@tcm.utcluj.ro

Abstract: Recent advances in laser technologies offer significant flexibility in the additive manufacturing domain. Extensive work was focused on material processing using laser-directed energy deposition for repairing parts. This pilot study investigated the use of selective laser melting (SLM) for depositing a superior material such as CoCr on an existing stainless steel base. The interface between these dissimilar materials was analyzed. During fabrication, both metals were gradually mixed in the liquid state as the first CoCr powder layer was melted on the steel base without obvious defects. According to SEM and EDAX, the heat-affected zone has a limited depth (<20 μm). XRD patterns recorded across the CoCr–304 interface show a homogenous mixture of γ(Fe) and α(Co) solid solutions. The microporosity calculated by CT was under 0.5%. Microhardness was measured at and near the interface region, showing that the intermixing zone has high hardness (470–480 HV1), which may be related to the fine-grained microstructure. Mechanical testing reveals that the adhesion strength at rupture is 35% higher compared with the ultimate tensile strength of 304 steel. This adhesion strength can be attributed to the complete melting of CoCr particles after laser irradiation and to the reduced thickness of the HAZ and the IZ.

Keywords: selective laser melting; CoCr; adhesion strength; microhardness; X-ray computed tomography; scanning electron microscopy



Citation: Cosma, C.; Teusan, C.; Gogola, P.; Simion, M.; Gabalcova, Z.; Trif, A.; Berce, P.; Balc, N. Investigation of the Interface between Laser-Melted CoCr and a Stainless Steel Substrate. *Metals* **2022**, *12*, 965. <https://doi.org/10.3390/met12060965>

Academic Editor: Francesca Borgioli

Received: 30 March 2022

Accepted: 30 May 2022

Published: 4 June 2022

Publisher's Note: MDPI stays neutral with regard to jurisdictional claims in published maps and institutional affiliations.



Copyright: © 2022 by the authors. Licensee MDPI, Basel, Switzerland. This article is an open access article distributed under the terms and conditions of the Creative Commons Attribution (CC BY) license (<https://creativecommons.org/licenses/by/4.0/>).

1. Introduction

Laser additive repair (LAR) can restore and modify prebuilt components, creating a metallurgical bond [1]. There are components conventional fabricated that suffer from wear, distortion, and cracks during their life cycle. Repairing these items is sometimes considered cost effective and time saving as opposed to replacing them [2–4]. To repair complex components, traditional methods cannot be used [3,5]. Therefore, LAR is an interesting approach to repair them.

Numerous LAR studies were focused on regeneration of damaged parts by multi-layer build up using similar materials for substrate and laser deposition. For example, Liu et al. used laser cladding to repair a rudder anti-rotation bracket and a landing gear shelf bracket for multi-role fighters (McDonnell Douglas F/A-18 Hornet) [6]. Marazani et al. studied the mechanical behavior and microstructure of a Ti6Al4V interface fabricated by LAR on cast Ti6Al4V [7,8]. Perini et al. used steel (C40) as a substrate carbon and irradiated 316L stainless steel powder [9]. Constantinescu et al. studied the localization of plastic

strain due to microstructure gradient on LAR structures, using a nickel alloy (Inconel 718) deposited on a wrought Inconel 718 substrate and 316 L stainless steel deposited on 316 substrates [10,11]. These LAR studies were developed using a laser cladding process, also known as direct energy deposition (DED).

Selective laser melting (SLM) can provide better design freedom and the ability to manufacture complex parts and control a wide range of parameters [5]. These benefits would improve LAR. Compared with DED, SLM can increase geometric precision and limit the heat-affected zone. Currently, SLM is used to fabricate functional parts made of titanium [12,13], stainless steel [14–17], and cobalt–chrome (CoCr) alloys [18–21]. There is, therefore, a need to investigate this alternative technology for LAR applications.

Moreover, to improve the physical-mechanical characteristics of a repaired component, SLM offers the possibility of applying a superior material on the damaged area. The interface between two dissimilar materials plays a prominent role in determining the overall performance of the processed component [5]. On this subject, limited SLM work is available. Some DED studies investigate the interface between two dissimilar materials, such as tool steel and cobalt-based alloys [3,18]. Information about welding dissimilar steels shows interesting findings on the behavior of weld interfaces. Literature sources indicate potential problems with the formation of brittle intermetallic phases as well as brittle solid solutions. Using Ni-based filler materials is a valid option to overcome these issues [19,20]. Due to its higher specific strength, wear resistance, and corrosion resistance, a CoCr alloy could be a viable solution to repair a stainless steel component. However, extended SLM studies are required to examine the performance of CoCr–steel interfaces.

The present work investigates the mechanical response and microstructure of CoCr laser melted on a stainless steel (AISI 304) substrate using SLM. The CoCr–304 interface was analyzed by X-ray computer tomography (CT), scanning electron microscopy (SEM), energy dispersive X-ray spectroscopy (EDAX), and X-ray diffractometry (XRD). The results expose the adhesion strength and microhardness of the CoCr–304 interface. The novelty of this study refers to the obtained adhesion strength value (838 MPa), and microstructure outcomes focused on the two dissimilar alloys SLM-processed.

2. Materials and Methods

2.1. Materials and Specimen Design

To explore the mechanical response of a laser-melted material on a conventional substrate, their thermal properties, such as thermal expansion coefficient and conductivity, should be closely evaluated. For this purpose, we examined different materials with good corrosion resistance. This study included AISI 304 stainless steel (SS) and a CoCr alloy because their thermal properties are similar (see Table 1).

Table 1. Thermal properties of 304 SS and CoCr.

Properties	Wrought 304 SS [21]	CoCr [22]
Density [g/cm ³]	8	8.8 *
Thermal expansion coefficient [$\mu\text{m}/\text{m} \times ^\circ\text{C}$]	17.2	14.3
Thermal Conductivity from 300 to 500 °C [$\text{W} \times \text{m}^{-1} \times ^\circ\text{C}^{-1}$]	14–17	13–22
Melting Point	1400–1455	1305–1400
Specific Heat from 0 to 100 °C [$\text{J}/\text{kg} \times \text{K}$]	490–530	450

* Density is expressed for SLM parts made of CoCr powder.

The most versatile and widely used SS available is AISI 304 [21,23,24]. It has good forming and welding characteristics. This stainless steel is also known as UNS S30400 (North America) or EN 1.4301 (Europe). This austenitic steel contains both chromium (18–18.79%) and nickel (8–8.5%). Using cold-rolled 304 bars, we manufactured two plates adapted for SLM (\varnothing 100 mm and 30 mm thickness). These plates were used as substrates, where CoCr powder was irradiated.

CoCr powder was purchased from Scheffter (Germany) and Table 2 shows its chemical composition according to the material data sheet. This powder is free of nickel, cadmium, beryllium, and lead. The spherical CoCr particles have a diameter between 10 and 45 μm and were obtained through a gas atomization process.

Table 2. Chemical composition of CoCr powder [22].

Chemical Element	Co	Cr	W	Mo	Si	Other Element (C, Fe, Mn, N)
Maximum weight percentage [%]	59.0	25.0	9.5	3.5	1	<1

The sample dimensions are detailed in Figure 1. To evaluate the adhesion strength between CoCr and the 304 substrate, the specimens were built vertically as shown in Figure 1. Practically, the CoCr part of the specimen represents half of a standard sample designed in concordance with ISO 6892 [25]. The interface area is 25 mm^2 .

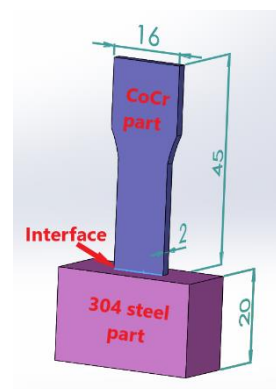


Figure 1. Virtual model of CoCr–304 specimen for mechanical testing (unit: mm).

2.2. SLM Parameters

To fabricate the CoCr–304 specimens, a Sisma MySINT 100 (Piovene Rocchette, Italy) was used. The system has two fiber laser sources up to 200 W. This technology allows lasers to work simultaneously, but each one scans a different part of the powder bed (Figure 2a). Taking into consideration the opto-mechanical calibration recommendations [26], the laser spot size was 30 μm . Based on our experience in SLM and previous studies, the process parameters were: 90 W laser power, 800 mm/s scanning speed, 60 μm space between two adjacent laser tracks (hatch distance), and 20 μm layer thickness [17,27–30]. These laser parameters were set up for both the outer boundary and hatch scanning. The density energy (E) applied to irradiate CoCr powder was 93.75 J/mm^3 , calculated by Equation (1):

$$E = \frac{P}{v \times h \times t} \left(\text{J}/\text{mm}^3 \right) \quad (1)$$

where P is the laser power (W), v is the scan speed (mm/s), h is the hatch spacing (mm) and t is the layer thickness (mm).

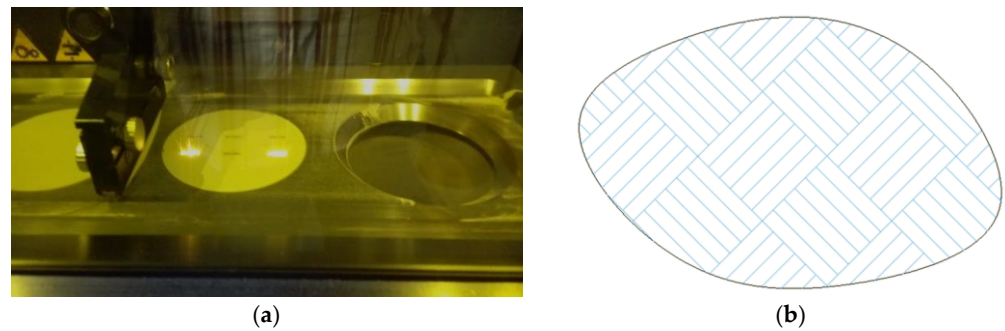


Figure 2. (a) Sisma equipment used to manufacture the specimens (dual laser technology); (b) island laser scanning applied on a slice.

For the scanning strategy, we selected “islands” (or chessboard). In Figure 2b, we present a sketch of islands laser scanning, where square islands have an area of $3 \times 3 \text{ mm}^2$ and scan vector directions are angular. According to the “layer by layer” principle and using the above mentioned SLM parameters, 12 CoCr specimens were melted directly on the 304 substrate. For comparison purposes, the other 12 standard specimens were SLM fabricated using CoCr powder (vertical build-up orientation). After SLM manufacturing, the specimens were exposed to a typical stress-relieving treatment ($880 \text{ }^\circ\text{C}$ for 1 h).

2.3. Mechanical Properties

To test the adhesion strength, tensile tests were performed. The mechanical behavior of specimens was measured using the Zwick Z100 universal testing system (ZwickRoell, Germany), in compliance with ISO 6892—Metallic materials—Tensile testing [25]. Working parameters of the Zwick system were 50% humidity at $18 \text{ }^\circ\text{C}$ and a 2 mm/min load rate. The fixing system was adapted for CoCr–304 samples as shown in Figure 3. The cross section of CoCr–304 jointing was $\sim 25 \text{ mm}^2$ and the following mechanical characteristics were measured: tensile adhesion strength at rupture, Young’s modulus, and elongation at fracture. To compare the results, the CoCr samples were also considered. For statistics, we calculated the standard deviation using Equation (2):

$$SD = \sqrt{\frac{\sum (X - \bar{X})^2}{N - 1}} \quad (2)$$

where SD is the standard deviation, X is the mechanical property measured, \bar{X} the mean of the mechanical property, and N is the number of trials. Twice the standard deviation means approximately 95% of measurements are in the confidence interval, ranging between the mean minus two times the standard deviation, and the mean plus two times the standard deviation.

Microhardness measurements were performed using a Vickers hardness tester (Wilson Tukon 1102; Buehler ITW Co, Lake Bluff, IL, USA). The surfaces were prepared using wet silicon carbide disks and abrasive papers. Microindentation hardness evaluations were developed by applying a force of 9.81 N across the CoCr–304 interface, according to ASTM E384-17 [31]. Twenty lines were analyzed, with a $200 \text{ }\mu\text{m}$ step. On each line, ten measurements were collected.

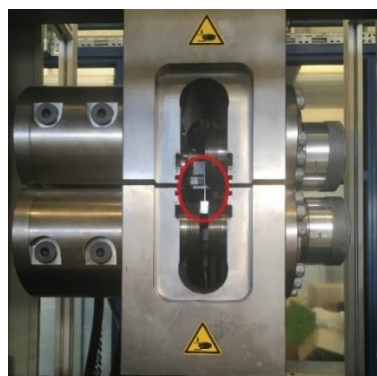
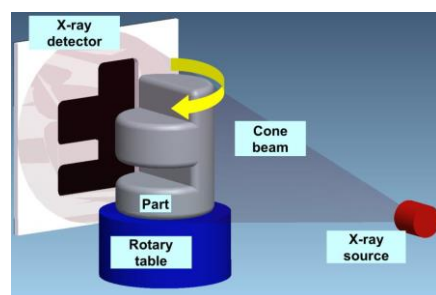


Figure 3. CoCr-304 specimen fixed using the ZwickRoell system during the tensile tests; the red circle marks the specimen.

2.4. CT Scanning

Due to the ability of X-rays to penetrate different materials, X-ray computed tomography (CT) is used in non-destructive evaluations and testing applications [32]. Typical industrial CT can be used to investigate flaws, such as voids or cracks, in particle analysis of materials, and to determine methodological aspects (nominal deviations or surface quality) [33]. The main components of industrial CT are a X-ray source, a X-ray detector, a kinematic systems for rotary table, reconstruction software, edge detection software and analysis software (Figure 4a) [34]. The maximum material thickness that can be penetrated by X-rays depends on the material attenuation coefficient and X-ray photon energy [33].



(a)



(b)

Figure 4. (a) Main components of an industrial CT [34]; (b) CT system of the type Nikon XT H 225.

In the present work, we used a CT system of the type Nikon XT H 225 (Figure 4b). The scanning parameters for CT are detailed in Table 3. Based on preliminary investigation, the authors found that these measurement settings offer the possibility to penetrate dense metals such as CoCr with a maximum 5 mm thickness. In this CT system, the specimens were rotated in the X-ray beam, while the X-ray source and the detector remained stationary. The software used to reconstruct the model and to analyze the CT scans was Volume Graphics myVGL 3.4 (Volume Graphics GmbH, Heidelberg, Germany).

Table 3. Measurement settings for the Nikon CT.

Parameter	Value
Filter material	Copper
Filter thickness	1.0 mm
Acceleration voltage	225 kV
Filament current	184 μ A
Exposure time	1415 ms
Number of projections	1440 per 360° rotation
Voxel size	17.3 μ m
Detector matrix (pixels)	1008 \times 1008

2.5. SEM, EDAX, and XRD

The metallographic preparation of the specimens includes standard grinding using abrasive papers and a polishing step on diamond pastes with various grain sizes (down to 1 μm). To analyze 3D print quality on a more significant area, the ZEISS LSM700 laser scanning confocal microscope (LSCM, Carl Zeiss AG, Oberkochen, Germany) was operated in the light microscopy mode. The interface area was investigated with a JEOL JSM 7600F scanning electron microscope (SEM, Jeol Ltd., Tokyo, Japan) with a Schottky field emission electron source, operating at 15 kV and 90 μA . Analysis of chemical elements was performed using the Oxford Instruments X-Max silicon drift detector and an energy dispersive X-ray spectrometer (EDAX, Oxford Instruments plc, Abingdon, UK). XRD was carried out on polished surfaces of the samples by the PANalytical Empyrean X-ray diffractometer (XRD) (Malvern Panalytical Ltd., Malvern, UK). The measurements were performed in Bragg–Brentano geometry. The XRD source was set to 40 kV and 40 mA. Phase quality was analyzed using PANalytical Xpert High Score program (HighScore Plus version 3.0.5) with the ICSD FIZ Karlsruhe database. For the CoCr side, quantitative phase composition was determined from XRD patterns, using the Rietveld refinement-based program MAUD version 2.84 [35]. The program uses an asymmetric pseudo-Voigt function to describe experimental peaks. An isotropic size–strain model was applied and a minor discrepancy between the nominal and measured peak intensities was corrected using the spherical harmonic functions with fiber symmetry. The quality of the fit was below 5% Rwp.

3. Results

3.1. Mechanical Response of the CoCr–304 Interface

In Figure 5, we show the SLM-fabricated specimens. To prepare the CoCr–304 specimens, the substrate was milled to obtain the required design. Mechanical testing was carried out on the CoCr–304 specimens and on standard CoCr samples. Representative stress–strain curves are plotted in Figure 6, and the determined properties are detailed in Table 4. Mechanical testing showed the anisotropic behavior of specimens due to the generative production principle also observed in other SLM studies [17,36,37].



Figure 5. (a) SLM-fabricated specimens to test the adhesion between CoCr and the 304 substrate. The specimens after stress relief heat treatment: (b) CoCr–304 specimens after mechanical testing.

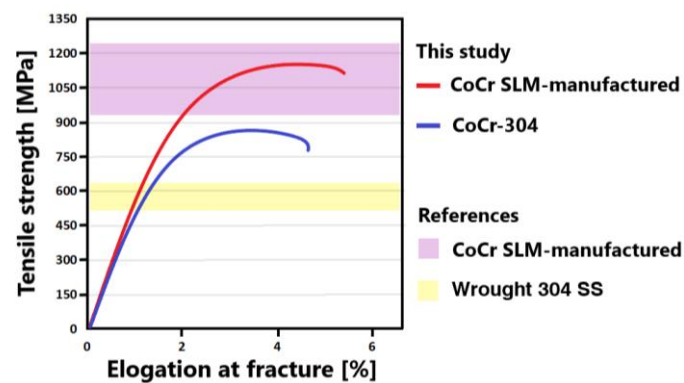


Figure 6. Mechanical response of SLM-fabricated CoCr-304 and CoCr specimens; Comparison with literature results (References) for wrought 304 SS [38–40] and SLM-fabricated CoCr [22,36,37,41].

Table 4. Adhesion strength between CoCr and 304 SS (mean \pm standard deviation).

Characteristic	CoCr-304	CoCr *
Adhesion strength at rupture [MPa]	838 (\pm 16.9)	1152 (\pm 36.7)
Young's modulus [Gpa]	157 (\pm 18.4)	174 (\pm 15.1)
Elongation at fracture [%]	4.6 (\pm 1.3)	5.2 (\pm 0.8)

* Mechanical properties of SLM-fabricated CoCr specimens in this study.

From our findings, the CoCr-304 specimens have a tensile adhesion strength at rupture of approximately 838 Mpa, Young's modulus of approximately 157 Gpa, and elongation at fracture of 4.6% (Table 4). The standard SLM-fabricated CoCr samples had an ultimate tensile strength of 1150 Mpa (vertical build-up orientation). Other studies using SLM determined a similar mechanical resistance or lower for CoCr alloys, ranging from 923 Ma to 1220 Mpa [36,37,41]. According to the material data sheet, the 304 SS substrate has the following mechanical properties: an ultimate tensile strength of 500 Mpa and an elastic modulus of 193 Gpa.

The results of the elastic modulus are interesting, since the elastic modulus for SLM-fabricated CoCr is higher (174–180 Gpa). The observed anisotropy primarily influenced ductility and secondly the elastic modulus, reducing it to 157 Gpa for the CoCr-304 specimens. Considering CT and SEM of internal porosities, the lower elastic modulus can be attributed to SLM. Such results require further studies for a better understanding of the underlying phenomenon, as well as exploitation for special applications that may require a lower elastic modulus.

3.2. CT

Common materials that can be penetrated by X-rays are steel, ceramic, plastic, aluminum, and titanium alloy [32,42]. Due to the high density (8–8.8 g/cm³) of the materials used, the CT parameters allow X-rays to penetrate to a maximum 5 mm depth in the CoCr and 304 steel alloy. Before mechanical testing, the CoCr-304 specimens were examined using CT. As mentioned before, even when SLM parameters are optimized, internal defects may emerge. This non-destructive method can show different forms of porosity that may be present in SLM-fabricated parts and at the CoCr-304 interface, identify the root cause of porosity and be used for parameter optimization and validation [43]. Pore distribution is random in the specimens and an example is shown in Figure 7. The determined microporosity was minimal (under 0.5%) with mean pore sizes of 30–70 μ m (Figure 7). The largest pore identified was in a CoCr part at 18 mm from the interface and 120 μ m in size. In addition to the total porosity, the largest pore, and pore distribution, another specification in LAR applications is the distance between pores relative to their size [44]. Figure 7b shows the presence of a total of 31 pores with an average volumetric porosity of 0.3%. All

the pores were analyzed automatically and the distance between each pore was larger than the diameter of the largest pore of the two under consideration.

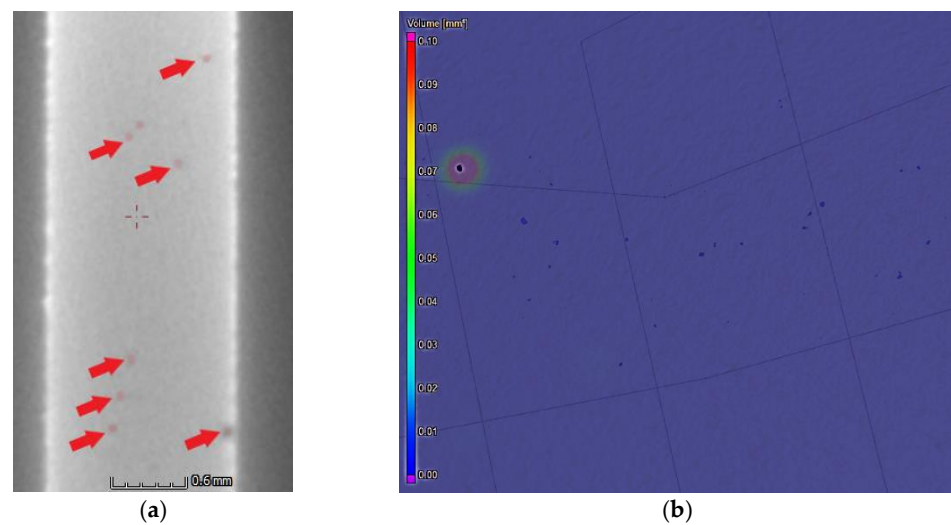


Figure 7. (a) Porosities identified in a CT image section of a CoCr-304 specimen (top section); the pores are marked with red to show their location (size is lower than 0.10 mm). (b) Virtual reconstruction of CoCr area; some random porosities were recorded up to 0.1 mm³ marked with blue.

Typical “as-built” surface roughness of a SLM part is shown in Figure 8a, where peaks and valleys with irregular steps can be seen. The voxel size is 17.3 μm and CT enabled us to detect undercuts and hidden irregularities at the CoCr-304 interface. In this study, these types of defects were not observed.

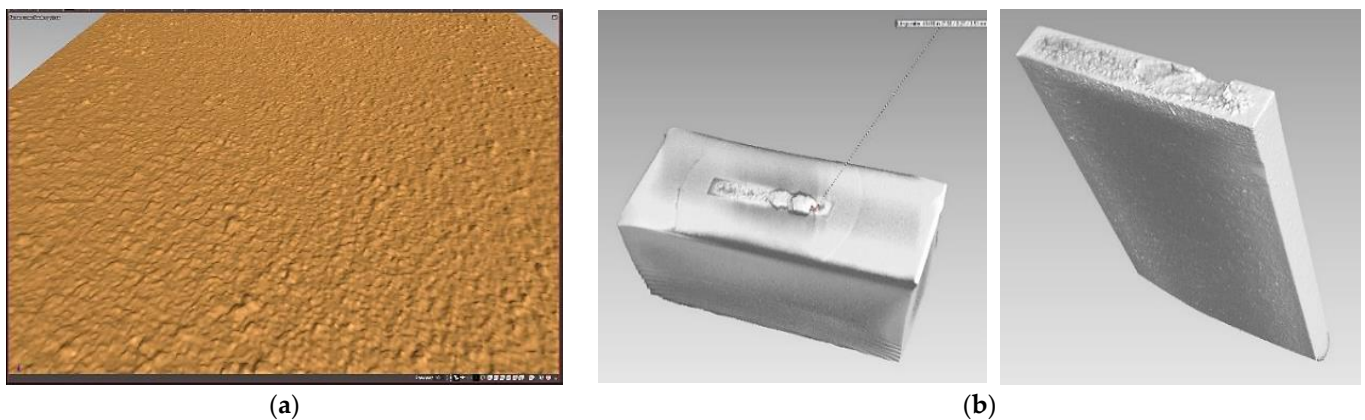


Figure 8. (a) Representative image of surface quality archived by laser melting of CoCr powder (SLM parameters are detailed in Section 2.2); (b) 3D reconstructions developed using CT images after mechanical testing.

Representative fractographs obtained after mechanical testing are detailed in Figures 9 and 10. The fractures were investigated using CT (sections and 3D reconstructions). The fractures have two dissimilar areas, a brittle zone, and a dumpling region. The brittle behavior is shown in Figure 9 where the CoCr part is analyzed. Considering this result and the EDAX maps (Section 3.3), we presume that the percent of Fe was high in the areas and this reduces the adhesion strength of the interface. Figure 9a indicates crack initiation between layers because the load direction is perpendicular to layer formation. The dumpling area of fracture is illustrated in Figure 10 and is a predominant region. During the adhesion rupture, shallow dimples are formed on quasi-cleavage facets with peaks between 0.06 and 0.30 mm (Figure 10a). As reported by several authors, the size

of the dimples reflects the typical cell dimensions of the solidification microstructure of SLM parts [37,45].

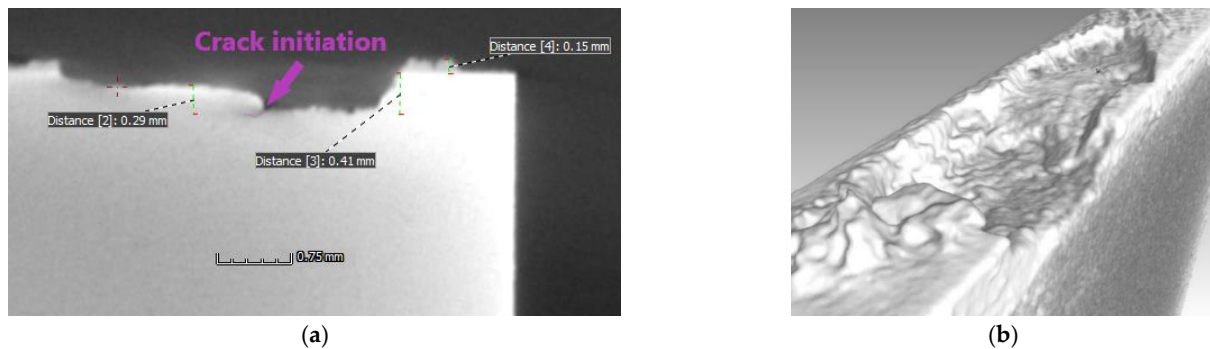


Figure 9. Fracture obtained in brittle area after mechanical testing (CoCr part): (a) CT section; (b) virtual reconstruction.

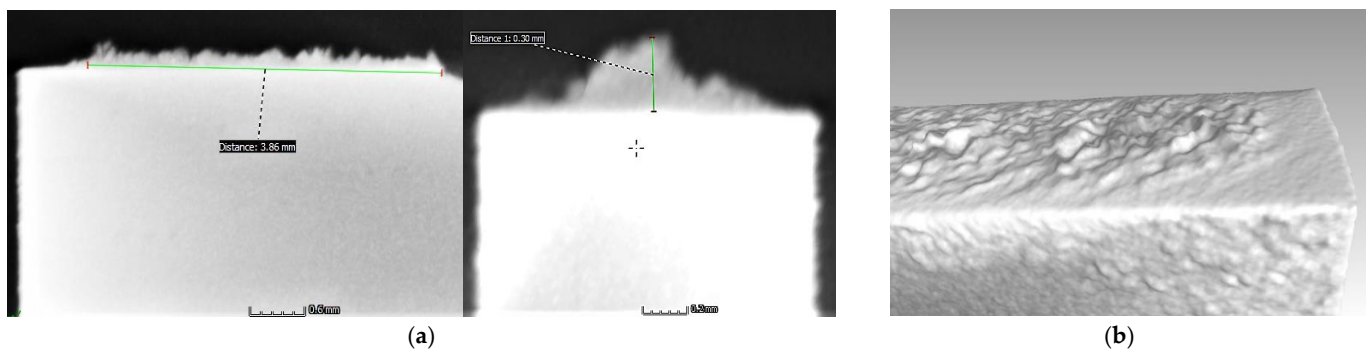


Figure 10. Fracture obtained in dumpling area after mechanical testing (CoCr part): (a) CT section; (b) virtual reconstruction.

3.3. Microstructure of the CoCr–304 Interface

SEM was focused on the interface between the CoCr alloy and AISI 304 steel (Figures 11–14). SEM images enable a clear distinction between the Co- and Fe-based areas (CoCr alloy and AISI 304 steel). Figure 11 shows the mixture of metals on their mutual interface. Even upon closer inspection (Figure 11b), no defects and/or sharp interfaces were detected. During SLM, both metals were gradually combined in the liquid state, as the first CoCr powder layers were melted on steel substrate. This was also confirmed by EDAX maps (Figure 12). Colors of the EDAX maps represent element concentrations in wt.%.

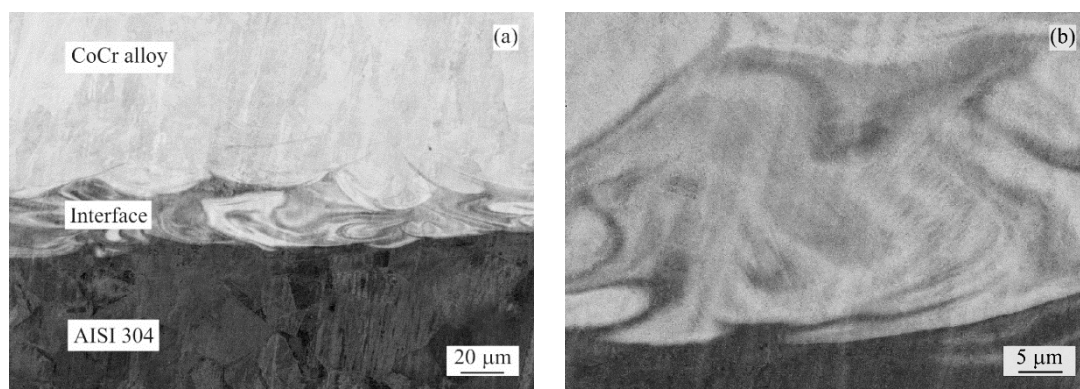


Figure 11. CoCr–304 steel interface: (a) overview; (b) detailed image ($\times 3000$ magnification).

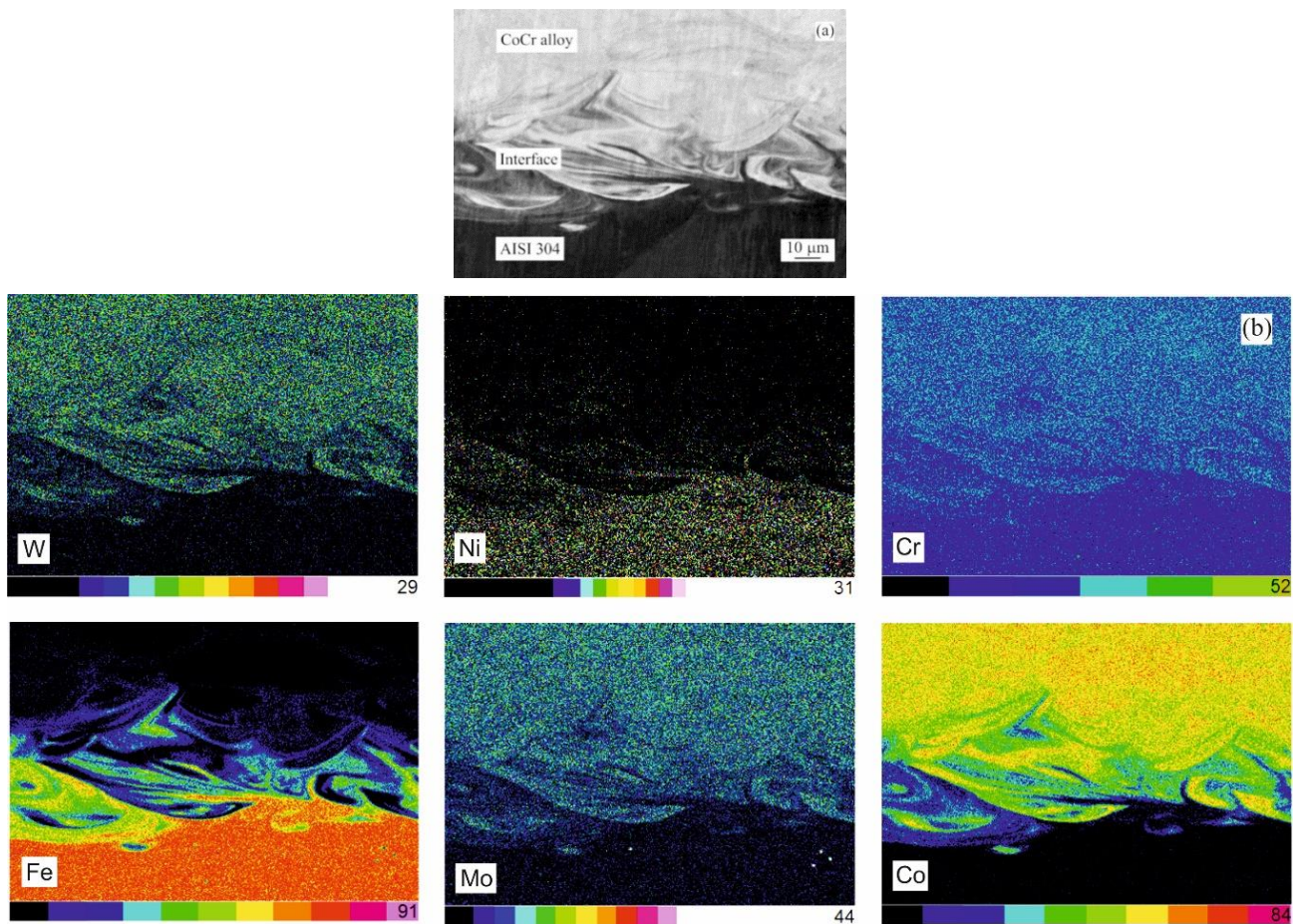


Figure 12. CoCr–304 interface maps based on main chemical elements (in wt.%) and their distribution: (a) SEM image; (b) EDAX maps for W, Ni, Cr, Fe, Mo, and Co.

Table 5. EDAX point measurement data for sites indicated in Figure 13. Red color indicates CoCr alloy composition; blue color indicates 304 stainless steel composition.

Site No./Chemical Elements (wt.%)	Si	Cr	Mn	Fe	Co	Ni	Mo	W
Spectrum 1	0.97	24.42	0.95	2.93	55.72	0.00	6.70	8.31
Spectrum 2	0.77	21.26	1.11	37.67	27.52	4.44	3.22	4.01
Spectrum 3	0.71	20.58	1.26	43.55	22.68	5.18	2.59	3.45
Spectrum 4	1.13	24.75	0.97	0.71	57.27	0.00	6.72	8.45
Spectrum 5	0.85	21.78	1.18	30.75	33.04	4.06	3.67	4.67
Spectrum 6	0.46	18.66	1.82	69.83	0.62	8.28	0.00	0.33

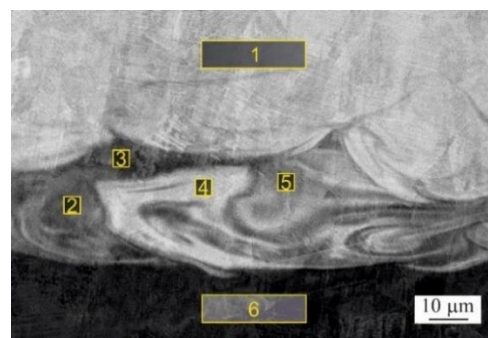


Figure 13. CoCr–304 interface in SEM image used for EDAX point measurements detailed in Table 5.

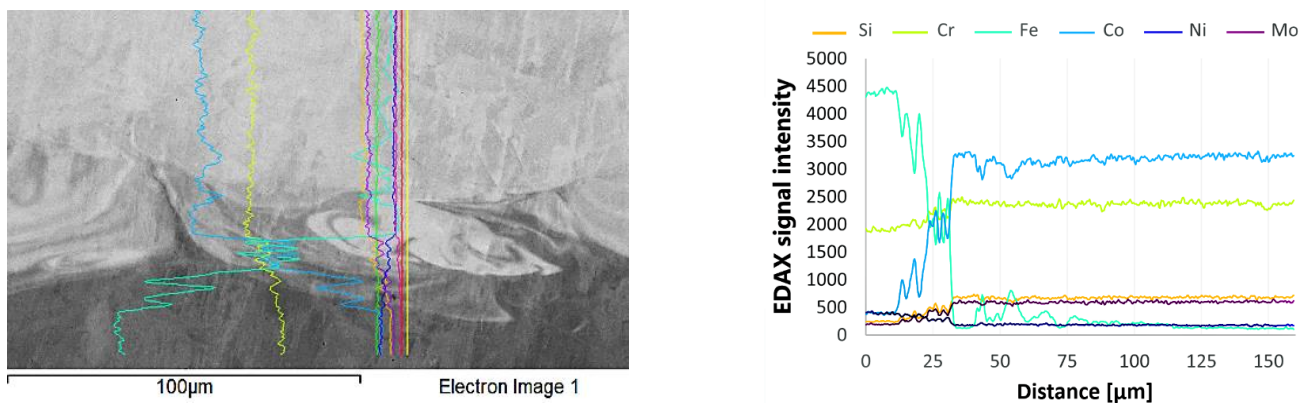


Figure 14. Chemical analysis at the CoCr–304 interface; chemical elements detected—tungsten (W), molybdenum (Mo), nickel (Ni), cobalt (Co), iron (Fe), magnesium (Mg), and chrome (Cr).

For a better understanding of the chemical composition, point measurements were performed on the indicated sites (Figure 13) and the results are listed in Table 5. Within the limitations of EDAX, we found Fe at 50–60 µm up from the 304 SS substrate, in the intermixing zone (Spectrum 1, Table 5). At approximately 150 µm from the 304 SS substrate, we detect only CoCr alloy composition. On the other hand, the composition of austenitic steel was recorded containing 18.6% chromium and 8.3% nickel (Spectrum 6, Table 5), which comply with the AISI 304 stainless steel standard [21].

Figure 14 shows the data acquired plotted in a chart with chemical analysis at the CoCr–304 interface, marking the main chemical elements—W, Mo, Ni, Co, Fe, Mg, and Cr. According to SEM and EDAX, the interface has two regions—a heat-affected zone (HAZ) and an intermixing zone (IZ). The HAZ has limited depth in the 304 substrate (lower than 20 µm; see Figures 11–14). The IZ has a thickness of approximately 70 µm. In total, the HAZ and the IZ range between 80 and 110 µm thickness in the CoCr–304 specimens (Figures 11–14).

3.4. XRD

The phase constitution of the Co–Cr alloy, AISI 304 steel and their common interface was studied by X-ray diffraction (XRD). The XRD patterns of all these areas are shown in Figure 15. Two phases were identified in the AISI 304 steel as shown in Figure 15a. The major phase was identified as γ (Fe), as we deal with an austenitic type of steel, and minor peaks were identified as α (Fe). The next XRD pattern was recorded across the CoCr–304 steel interface (Figure 15b). In this XRD pattern, the two main peaks correspond to two phases, namely γ (Fe) and α (Co). These two phases have very similar XRD patterns and are completely overlapping. No other phases were detected using XRD. The last pattern corresponds to the SLM-fabricated CoCr alloy (Figure 15c). The 3D printed part is formed mainly by the α (Co) solid solution, and the minor peaks indicate the presence of a ϵ (Co) solid solution.

3.5. Hardness Measurements

Twenty-one indentations were made across the substrate, interface, and CoCr region, with the first ten lines made on the steel substrate and the eleventh made in the HAZ. The twelfth indent was made near the intermixing zone and another nine on the CoCr side. Within the limitations of precise detection of the HAZ and intermixing lines, a graph of the microhardness measurements is presented in Figure 16. The Vickers hardness of the CoCr–304 interface was determined considering the HAZ and the IZ. The substrate of specimens made of 304 SS have a hardness of 216 HV with limited standard deviations (± 38 HV). CoCr powder laser melted on this substrate has a hardness of 453 HV with a standard deviation of ± 58 HV. Near the IZ, the highest hardness is 483 HV and was recorded due to a substitutional solid solution strengthening in the intermixing zone. The

hardness obtained in the HAZ is approximately 451 HV with a high standard deviation (± 87 HV). Statistically significant differences were observed among the groups ($p < 0.05$) for microhardness.

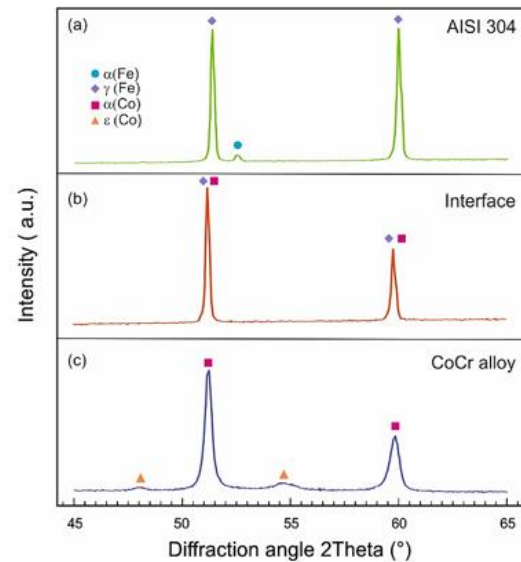


Figure 15. XRD patterns measured on specimen: (a) AISI 304 steel; (b) interface; (c) CoCr alloy.

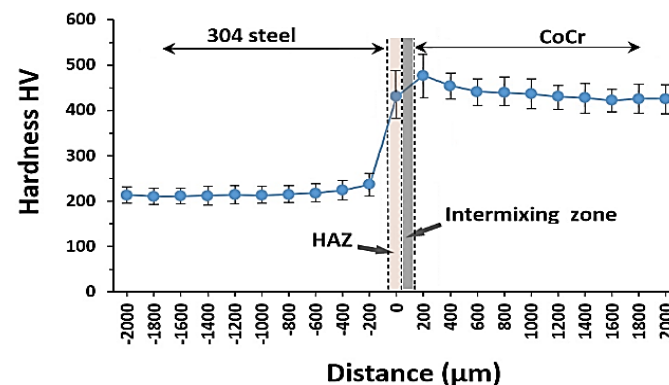


Figure 16. Vickers hardness of the CoCr–304 steel interface.

4. Discussion

A vertical orientation is the most common build-up strategy in SLM production because it allows for the placement of multiple parts on the machine platform, providing reduced surface roughness on vertical walls. On the other hand, it is well known that if the load direction is normal to layer formation, the mechanical resistance is lower. For this reason, the tensile adhesion strength of the CoCr–304 specimen is limited to 838 MPa (see Table 4). The building direction of the CoCr–304 specimens was chosen to be vertical because we aim to determine the minimum adhesion strength between these two metals. Improved adhesion strength can be obtained if the build-up direction is parallel to the layer structure (horizontal orientation of SLM part on 304 steel substate). Future work should investigate the impact of building orientation on adhesion strength. Our mechanical testing showed that the adhesion strength at rupture is 35% higher compared to the ultimate tensile strength of 304 steel (see Figure 6). Moreover, fracture surfaces observed after mechanical testing have a predominant dimple structure and a brittle area propagated by crack initiation in the CoCr layer structure (Figures 11–14).

The ability to detect porosity and internal voids in SLM parts was investigated in detail and similar results were reported previously [33,43].

The CoCr alloy was chosen as its primary solid solution was indicated to be compatible with the currently investigated steel (AISI 304) [3,18]. Based on SEM images, the interface shows a homogenous mixture of the two main alloys in the melted area. Both SEM and XRD show that no brittle intermetallic phases were observed. The primary phase in the AISI 304 steel is a $\gamma(\text{Fe})$ solid solution with a FCC crystal structure that has a crystal lattice parameter of 3.618 Å, while the main phase of the CoCr alloy is very similar. The $\alpha(\text{Co})$ solid solution also has a FCC crystal structure with a lattice parameter of 3.566 Å, which was confirmed by the significantly overlapping XRD patterns (Figure 15b). The similar crystal lattices enables perfect mixing of these two alloys. SEM demonstrates that the interface area has a limited thickness, which is between 80 and 110 μm . Compared with other DED studies, the HAZ thickness obtained in this study is lower [3,9,11,18,46,47]. A similar interface thickness was reported between a SLM-fabricated nickel alloy and a cast iron substrate [5].

Table 6 summarizes some reported efforts focused on the adhesion strength and hardness of the interface between base materials such as steels and deposition materials such as CoCr, Inconel, and 316L SS. Two different technologies were considered to repair steel components: SLM and DED. As we argued above, the published studies are mainly used DED. To the best of our knowledge, this is the first SLM study which analyzes the adhesion strength and interface between these two dissimilar alloys.

Table 6. Comparison of the adhesion strength and hardness obtained using different manufacturing methods to repair steel components.

Method	Substrate Material	Deposition Material	Laser Power [W]	Scanning Speed [mm/s]	Powder Thickness [mm]	Vickers Hardness [HV] *	Adhesion Strength [MPa]	Ref./Year
SLM	304 SS	CoCr	90	800	0.02	451–483	838	<i>This study</i>
SLM	Cast iron	Inconel 625	200	N/A	0.06	330–400	N/A	[5]/2018
DED	H13 tool steel	CoCr	350	3.7	0.60	520–650	618–624	[3]/2019
	304L SS	Inconel 625	910	N/A	N/A	210–250	N/A	[47]/2016
	316L SS	Inconel 718	450–750	4.0	0.55–0.80	140–180	530–595	[46]/2014
	Carbon steel C40	316L SS	N/A	N/A	N/A	220–510	N/A	[9]/2019
	316L SS	316L SS	225	33.3	0.12	180–225	430	[11]/2020
	Cast iron	EuTroLoy 16006 (Co-based alloy)	634–1671	2–6.67	N/A	490–600	N/A	[18]/2007

* Vickers hardness measured on interface: heat-affected zone (HAZ) and intermixing zone (IZ); DED—direct energy deposition; SLM—selective laser melting; SS—stainless steel; Inconel is an austenitic nickel-chromium-based superalloy; N/A indicates that the value is not available.

Depending on the deposition material, processing technology and parameters used, the adhesion strength varied from 430 to 624 MPa (Table 6). For example, Zhang et al. investigated the feasibility of DED using a H13 hot work tool with steel as a base and a CoCr alloy (Wallex 50) as deposition material for repairing molds to assure longer wear and corrosive life [3]. The laser power for this work was 350 W and the scanning speed 3.7 mm/s, obtaining an adhesion strength of 624 MPa and a microhardness at interface ranging from 520 to 650 HV1. SLM and the proposed processing parameters resulted in a higher adhesion strength compared to other research (see Table 6). Regarding the hardness of the interface region, the hardness determined is in accordance with other reports where SLM and DED were used [5,9,18].

The study results demonstrated that the advantages of CoCr deposition using SLM on 304 SS base are as follows: minimal distortion, a reduced heat-affected zone, low porosity, few microcracks in the interface structure, and superior adhesion strength. This information on the mechanical response between CoCr and 304 steel is relevant for future LAR applications.

Recent developments in digital fabrication technologies have made LAR possible and economically profitable [48,49]. Existing SLM machines can implement LAR to restore and modify prebuilt components creating a suitable metallurgical bond between an existing

304 stainless steel part and a CoCr deposition material. Due to its benefits, this technology has tremendous potential to be adopted by companies and to generate advanced laser additive reparations, improving the life cycle of metal reconstructed components [50–55]. Technology can also be used to fabricate functionally graded materials or to develop smart structures [56].

We believe that the proposed LAR approach paves the way to reducing the need to maintain a large inventory of 304 steel spare components, which would result in a reduction in cost and waste. Because CoCr alloys possess improved tensile strength and corrosion resistance compared with 304 stainless steel, with an adhesion strength of 830 MPa, the repaired parts may have an increased lifetime. Future studies should analyze the fatigue life and wear resistance of 304 steel parts repaired using LAR and a CoCr alloy.

5. Conclusions

The feasibility of SLM for depositing a superior material such as CoCr on an existing 304 stainless steel base was investigated. This pilot study analyzed the microstructure and chemical composition of the interface formed between these dissimilar materials. According to SEM and EDAX, the interface has a reduced thickness and the HAZ is limited ($<20\ \mu\text{m}$). The IZ has a thickness of approximately $70\ \mu\text{m}$ and has high hardness (470–480 HV1). Compared to in welding processes or DED, the HAZ thickness is lower. XRD patterns recorded across the CoCr–304 interface show a homogenous mixture of $\gamma(\text{Fe})$ and $\alpha(\text{Co})$ solid solutions. Perfect mixing of the CoCr alloy and AISI 304 steel was achieved in the melted area using the proposed SLM parameters. The similar crystal structures of the two main solid solutions predicts the formation of coherent interfaces between these two materials. No intermetallic-phase particles were observed by SEM, nor XRD, which could negatively influence the mechanical properties. CT determined the total porosity, the largest pore, and pore distribution.

The study results show that the stated configuration of the SLM parameters lead to limited microporosity in the CoCr–304 interface and a higher adhesion strength when compared to other reports. Mechanical testing reveals that the adhesion strength at rupture is 830 MPa and the fractures contain predominant dimpling regions. This notable adhesion strength can be attributed to the complete melting of CoCr particles after laser irradiation and to the reduced thickness of the HAZ and the IZ.

Author Contributions: Conceptualization, C.C., C.T. and N.B.; methodology, C.C. and N.B.; investigation, C.C., C.T., P.G., M.S., Z.G. and A.T.; supervision, P.B. and N.B.; writing—original draft, C.C., P.G. and N.B.; research funding, C.T., C.C. and P.B. All authors have read and agreed to the published version of the manuscript.

Funding: This work was supported by a grant from the Ministry of Research, Innovation and Digitalization CNCS-UEFISCDI, project number PN-III-P1-1.1-PD-2021-0326 within PNCDI III. This work was also supported by the Human Capital Operational Program agreement POCU/380/6/13/123927 financed from the European Social Fund (contract no. 56437/24.07.2019).

Data Availability Statement: Not applicable.

Conflicts of Interest: The authors declare no conflict of interest.

References

1. Lachmayer, R.; Lippert, R.B.; Fahlbusch, T. *3D-Druck Beleuchtet—Additive Manufacturing auf dem Weg in die Anwendung*; Springer: Berlin/Heidelberg, Germany, 2016; ISBN 978-3-662-49055-6.
2. Zghair, Y.A.; Lachmayer, R. Additive repair design approach: Case study to repair aluminium base components. In Proceedings of the 21st International Conference on Engineering Design, Vancouver, BC, Canada, 21–25 August 2017.
3. Zhang, X.; Pan, T.; Li, W.; Liou, F. Experimental Characterization of a Direct Metal Deposited Cobalt-Based Alloy on Tool Steel for Component Repair. *JOM* **2019**, *71*, 946–955. [[CrossRef](#)]
4. Xie, W.; Jiang, W.; Wu, Y.; Song, H.; Deng, S.; Lăzărescu, L.; Zhang, S.; Banabic, D. Process parameter optimization for thin-walled tube push-bending using response surface methodology. *Int. J. Adv. Manuf. Technol.* **2022**, *118*, 3833–3847. [[CrossRef](#)]

5. Sebastian, R.; Singh, A.K.; Paliwal, M.; Gautam, A. Investigation of the interface between SLM processed nickel alloy on a cast iron substrate. *Prog. Addit. Manuf.* **2019**, *4*, 131–142. [[CrossRef](#)]
6. Liu, Q.; Djugum, R.; Sun, S.; Walker, K.; Choi, Y.; Brandt, M. Repair and manufacturing of military aircraft components by additive manufacturing technology. In Proceedings of the 17th Australian Int. Aerospace Congress (AIAC 2017), Melbourne, VIC, Australia, 26–28 February 2017; pp. 363–368.
7. Marazani, T. Laser Additive Manufacturing Technology for Crack Repairs in Titanium Alloy Components. Ph.D. Thesis, University of Johannesburg, Johannesburg, South Africa, 2016.
8. Marazani, T.; Madyira, D.M.; Akinlabi, E.T. Laser Re-Melt Technique for Laser Additive Repair of Narrow Rectangular Cracks in Grade 5 Titanium Alloy (Ti-6Al-4V). *Key Eng. Mater.* **2019**, *796*, 129–136. [[CrossRef](#)]
9. Perini, M.; Amirabdollahian, S.; Bosetti, P. Building Multi-Material components by Direct Laser Deposition. *MATEC Web Conf.* **2019**, *299*, 01006. [[CrossRef](#)]
10. Guévenoux, C.; Hallais, S.; Charles, A.; Charkaluk, E.; Constantinescu, A. Mechanical response of a Laser Cladding repaired structure: Localization of plastic strain due to microstructure gradient. *MATEC Web Conf.* **2019**, *300*, 03003. [[CrossRef](#)]
11. Balit, Y.; Guévenoux, C.; Tanguy, A.; Upadhyay, M.; Charkaluk, E.; Constantinescu, A. High resolution digital image correlation for microstructural strain analysis of a stainless steel repaired by Directed Energy Deposition. *Mater. Lett.* **2020**, *270*, 127632. [[CrossRef](#)]
12. Armencea, G.; Berce, C.; Rotaru, H.; Bran, S.; Stefan, V.; Leordean, D.; Jula, C.-A.; Gheban, D.; Lazar, M.; Baciut, G.; et al. Titanium alloys with hydroxyapatite or SiO₂+TiO₂ coatings used in bone reconstruction. *J. Optoelectron. Adv. Mat.* **2015**, *9*, 865–868.
13. Zhao, D.; Huang, Y.; Ao, Y.; Han, C.; Wang, Q.; Li, Y.; Liu, J.; Wei, Q.; Zhang, Z. Effect of pore geometry on the fatigue properties and cell affinity of porous titanium scaffolds fabricated by selective laser melting. *J. Mech. Behav. Biomed. Mater.* **2018**, *88*, 478–487. [[CrossRef](#)]
14. Garcia-Lopez, E.; Siller, H.R.; Rodríguez, C.A. Development of AISI 316L stainless steel coronary stent. In *Laser-Based Micro-and Nanoprocessing XII*; International Society for Optics and Photonics: Bellingham, WA, USA, 2018. [[CrossRef](#)]
15. Grobelny, P.; Furmanski, L.; Legutko, S. Investigations of Surface Topography of Hot Working Tool Steel Manufactured with the Use of 3D Print. *MATEC Web Conf.* **2017**, *137*, 02004. [[CrossRef](#)]
16. Buican, G.R.; Oancea, G.; Martins, R.F. Study on SLM manufacturing of teeth used for dental tools testing. *MATEC Web Conf.* **2017**, *94*, 03002. [[CrossRef](#)]
17. Cosma, C.; Kessler, J.; Gebhardt, A.; Campbell, I.; Balc, N. Improving the Mechanical Strength of Dental Applications and Lattice Structures SLM Processed. *Materials* **2020**, *13*, 905. [[CrossRef](#)]
18. Ocelik, V.; de Oliveira, U.; de Boer, M.; de Hosson, J.T.M. Thick Co-based coating on cast iron by side laser cladding: Analysis of processing conditions and coating properties. *Surf. Coat. Technol.* **2007**, *201*, 5875–5883. [[CrossRef](#)]
19. Dak, G.; Sirohi, S.; Pandey, C. Study on microstructure and mechanical behavior relationship for laser-welded dissimilar joint of P92 martensitic and 304L austenitic steel. *Int. J. Press. Vessel. Pip.* **2022**, *196*, 104629. [[CrossRef](#)]
20. Sirohi, S.; Taraphdar, P.K.; Dak, G.; Pandey, C.; Sharma, S.; Goyal, A. Study on evaluation of through-thickness residual stresses and microstructure-mechanical property relation for dissimilar welded joint of modified 9Cr-1Mo and SS304H steel. *Int. J. Press. Vessel. Pip.* **2021**, *194*, 104557. [[CrossRef](#)]
21. Materials Properties of 304 Stainless Steel. Available online: <http://asm.matweb.com/search/SpecificMaterial.asp?bassnum=mq304a> (accessed on 1 August 2021).
22. Material Data Sheet for CoCr Powder Starbond CoS 30. S&S Scheftner GmbH, Germany. Available online: www.scheftner.dental (accessed on 8 August 2021).
23. Popan, I.A.; Balc, N.; Popan, A.; Fratila, D.; Trif, A. Surface roughness prediction during dry turning of austenitic stainless steel AISI 304. *Appl. Mech. Mater.* **2015**, *808*, 54–59. [[CrossRef](#)]
24. Pustan, M.; Chiorean, R.; Birleanu, C.; Dudescu, C.; Muller, R.; Baracu, A.; Voicu, R. Reliability design of thermally actuated MEMS switches based on V-shape beams. *Microsyst. Technol.* **2017**, *23*, 3863–3871. [[CrossRef](#)]
25. ISO 6892-1:2019; Metallic Materials—Tensile Testin—Part 1: Method of Test at Room Temperature. ISO: Geneva, Switzerland, 2019.
26. Godineau, K.; Lavernhe, S.; Tournier, C. Calibration of galvanometric scan heads for additive manufacturing with machine assembly defects consideration. *Addit. Manuf.* **2019**, *26*, 250–257. [[CrossRef](#)]
27. Yan, X.; Lin, H.; Wu, Y.; Bai, W. Effect of two heat treatments on mechanical properties of selective-laser-melted Co-Cr metal-ceramic alloys for application in thin removable partial dentures. *J. Prosthet. Dent.* **2018**, *119*, e1–e6. [[CrossRef](#)]
28. Cosma, C.; Moldovan, M.; Simion, M.; Balc, N. Impact of laser parameters on additively manufactured cobalt-chromium restorations. *J. Prosthet. Dent.* **2021**. [[CrossRef](#)]
29. Kim, H.R.; Jang, S.H.; Kim, Y.K.; Son, J.S.; Min, B.K.; Kim, K.-H.; Kwon, T.Y. Microstructures and mechanical properties of Co-Cr dental alloys fabricated by three CAD/CAM-based processing techniques. *Materials* **2016**, *9*, 596. [[CrossRef](#)]
30. Ucar, Y.; Ekren, O. Effect of layered manufacturing techniques, alloy powders, and layer thickness on mechanical properties of Co-Cr dental alloys. *J. Prosthet. Dent.* **2018**, *120*, 762–770. [[CrossRef](#)] [[PubMed](#)]
31. ASTM E384-17; Standard Test Method for Microindentation Hardness of Materials. American Society for Testing and Materials: West Conshohocken, PA, USA, 2018.

32. Angheluta, L.M. 3D reconstruction of archaeological artefacts from 2-D X-ray images. *Optoelectron. Adv. Mater.—Rapid Commun.* **2018**, *12*, 705–712.
33. De Chiffre, L.; Carmignato, S.; Kruth, J.P.; Schmitt, R.; Weckenmann, A. Industrial applications of computed tomography. *CIRP Ann.* **2014**, *63*, 655–677. [[CrossRef](#)]
34. Angel, J.A.B. Quality Assurance of CT Scanning for Industrial Applications. Ph.D. Thesis, Technical University of Denmark, Kongens Lyngby, Denmark, 2014.
35. Lutterotti, L.; Matthies, S.; Wenk, H.R. MAUD (Material Analysis Using Diffraction): A user friendly Java program for rietveld texture analysis and more. In Proceedings of the 12th International Conference on Textures of Materials (ICOTOM-12), Montreal, QC, Canada, 9–13 August 1999; Available online: <http://hdl.handle.net/11572/57067> (accessed on 22 August 2021).
36. Zhou, Y.; Li, N.; Yan, J.; Zeng, Q. Comparative analysis of the microstructures and mechanical properties of Co-Cr dental alloys fabricated by different methods. *J. Prosthet. Dent.* **2018**, *120*, 617–623. [[CrossRef](#)]
37. Liverani, E.; Balbo, A.; Monticelli, C.; Leardini, A.; Belvedere, C.; Fortunato, A. Corrosion resistance and mechanical characterization of ankle prostheses fabricated via selective laser melting. *Procedia CIRP* **2017**, *65*, 25–31. [[CrossRef](#)]
38. Material Data Sheet for 304 Stainless Steel. Otel Inox, Romania. Available online: www.otelinox.com/ro/products/304.asp (accessed on 3 August 2021).
39. Milad, M.; Zreiba, N.; Elhalouani, F.; Baradai, C. The effect of cold work on structure and properties of AISI 304 stainless steel. *J. Mater. Process. Technol.* **2008**, *203*, 80–85. [[CrossRef](#)]
40. Shojaati, M.; Beidokhti, B. Characterization of AISI 304/AISI 409 stainless steel joints using different filler materials. *Constr. Build. Mater.* **2017**, *147*, 608–615. [[CrossRef](#)]
41. Hitzler, L.; Alifui-Segbaya, F.; Williams, P.; Heine, B.; Heitzmann, M.; Hall, W.; Merkel, M.; Öchsner, A. Additive Manufacturing of Cobalt-Based Dental Alloys: Analysis of Microstructure and Physicomechanical Properties. *Adv. Mater. Sci. Eng.* **2018**, *2018*, 8213023. [[CrossRef](#)]
42. Musteata, A.E.; Pelin, G.; Botan, M.; Popescu, A.; Deleanu, L. The Behavior of Polymeric Blends (PP + PA6) in Tensile Tests. *Mater. Plast.* **2020**, *57*, 153–166. [[CrossRef](#)]
43. Du Plessis, A.; Le Roux, S.G. X-ray micro-CT supporting the South African Additive Manufacturing Community. *Preprints* **2018**, *1*, 2018100534. [[CrossRef](#)]
44. Du Plessis, A.; Sperling, P.; Beerlink, A.; Tshabalala, L.; Hoosain, S.; Mathe, N.; Le Roux, S.G. Standard method for microCT-based additive manufacturing quality control 1: Porosity analysis. *Methods X* **2018**, *5*, 1102–1110. [[CrossRef](#)]
45. Čapek, J.; Machová, M.; Fousová, M.; Kubásek, J.; Vojtěch, D.; Fojt, J.; Jablonska, E.; Lipov, J.; Ruml, T. Highly porous, low elastic modulus 316L stainless steel scaffold prepared by selective laser melting. *Mater. Sci. Eng. C* **2016**, *69*, 631–639. [[CrossRef](#)] [[PubMed](#)]
46. Shah, K.; Haq, I.; Khan, A. Parametric study of development of Inconel-steel functionally graded materials by laser direct metal deposition. *Mater. Des.* **2014**, *54*, 531–538. [[CrossRef](#)]
47. Carroll, B.E.; Otis, R.A.; Borgonia, J.; Suh, J.O.; Dillon, P.; Shapiro, A.A.; Hofmann, D.C.; Liu, Z.K.; Beese, A.M. Functionally graded material of 304L stainless steel and Inconel 625 fabricated by directed energy deposition: Characterization and thermodynamic modeling. *Acta Mater.* **2016**, *108*, 46–54. [[CrossRef](#)]
48. Pradel, P.; Campbell, R.I.; Balc, N.O. A taxonomy of customers’ characteristics influencing product personalisation. *Proc. Rom. Acad. Ser. A—Math. Phys. Tech. Sci.* **2021**, *22*, 153–161.
49. Ghosh, P.S.; Sen, A.; Chattopadhyaya, S.; Sharma, S.; Singh, J.; Dwivedi, S.P.; Saxena, A.; Khan, A.M.; Pimenov, D.Y.; Giasin, K. Prediction of Transient Temperature Distributions for Laser Welding of Dissimilar Metals. *Appl. Sci.* **2021**, *11*, 5829. [[CrossRef](#)]
50. Aversa, A.; Lorusso, M.; Trevisan, F.; Ambrosio, E.P.; Calignano, F.; Manfredi, D.; Biamino, S.; Fino, P.; Lombardi, M.; Pavese, M. Effect of Process and Post-Process Conditions on the Mechanical Properties of an A357 Alloy Produced via Laser Powder Bed Fusion. *Metals* **2017**, *7*, 68. [[CrossRef](#)]
51. Curaj, A.; Paunica, M.; Popa, A.; Holeab, C.; Jora, O.D. Sustainability Through Directed Change in the Visionary University: From Predicting to Producing the Future. *Amfiteatru Econ.* **2020**, *22*, 905–919. [[CrossRef](#)]
52. Miron-Borzan, C.S.; Sabau, E.; Vilau, C.; Ceclan, V. A comparative study using finite element analyses for cervical disc implants. *Acad. J. Manuf. Eng.* **2020**, *18*, 5–11.
53. Monkova, K.; Vasina, M.; Monka, P.P.; Vanca, J.; Kozak, D. Effect of 3D-Printed PLA Structure on Sound Reflection Properties. *Polymers* **2022**, *14*, 413. [[CrossRef](#)] [[PubMed](#)]
54. Dobransky, J.; Kocisko, M.; Baron, P.; Simkulet, V.; Behalek, L.; Vojnova, E.; Novakova, L. Evaluation of the impact energy of the samples produced by the additive manufacturing technology. *Metalurgija* **2016**, *55*, 477–480.
55. Mukherjee, T.; Zuback, J.; De, A. Printability of alloys for additive manufacturing. *Nat. Sci. Rep.* **2016**, *6*, 19717. [[CrossRef](#)] [[PubMed](#)]
56. Torims, T.; Brückner, F.; Ratkus, A. Additive manufacturing in-situ repair solutions for the FCC. In *FCC Weekend*; Riga Technical University: Riga, Latvia, 2018.